Parameter Design for a High-Speed Permanent Magnet Machine under Multiphysics Constraints

Guanghui Du, Na Huang, Gang Lei, *Member, IEEE,* Jianguo Zhu, *Senior Member, IEEE*

***Abstract*—Regarding high-speed permanent magnet machines (HSPMMs), there is a lack of complete and detailed design processes for main parameters under multiphysics constraints, which makes it difficult to obtain high-reliability designs. This paper presents a detailed and complete design process for the main parameters of an HSPMM under multiphysics constraints. Firstly, the initial sizes are obtained through electromagnetic and mechanical design theory. Then, the influence of design parameters on rotor stress is analyzed in detail, including PM material, rotor temperature, sleeve thickness, PM thickness and rotor diameter. Furthermore, the rotor dynamics have also been studied in detail, including the effects of bearing stiffness, impeller mass, rotor diameter, core length, and gyroscopic effect on critical speed. Afterwards, the comprehensive research on the electromagnetic filed and the loss characteristics is performed. The cooling system is designed and the thermal field is also studied in Ansys-Cfx. Besides，the coupled temperature-stress analysis is established considering the interaction between temperature and mechanical characteristics. Finally, a full-size HSPMM prototype has been fabricated and tested to validate the detailed multiphysics design process.**

***Index Terms*—High-speed permanent magnet machine, multiphysics, thermal analysis, rotor stress, rotor dynamics.**

I. Introduction

The direct drive high-speed permanent magnet machine (HSPMM) has been widely used in compressors, gas turbines, distributed power generation, and flywheels, *etc*., for its various advantages of high power, small size and low weight, and so on [1]-[3]. By removing the mechanical gearbox, the size and weight of the drive system can be further reduced, and also the efficiency, noise and reliability of the HSPMM can be greatly improved [4]-[6]. Because of the high operating speed, the structure, performance, and hence application of HSPMMs are subject to various vital factors, including the rotor mechanical stress and dynamics, electromagnetic field distribution and power losses, and high temperature in relation to the material and structure [7], [8].

In general, a small rotor diameter is usually chosen in order to improve the rotor mechanical strength when operated at high speeds [9], [10]. However, the small rotor diameter leads to a long core length according to the classical theory of machine design, which could reduce the critical speed of the machine [11], [12]. When the critical speed is close to the operating speed, resonances may happen [13], which may deform or even damage the rotor of the HSPMM [14]. Therefore, it is essential to determine the rotor length and diameter through a comprehensive study to avoid rotor bending resonances [15].

Sintered permanent magnets (PMs) are usually used to further improve the power density of HSPMM. Due to the low tensile strength of sintered PM [16], [17], a high strength sleeve made of carbon fibre or a nonmagnetic alloy is usually adopted to ensure the operational safety at high speeds [18]. Compared with alloy, the carbon fibre sleeve has proved to be a better choice due to its low electrical conductivity and hence low eddy current loss [19]. While a thick sleeve can improve effectively the rotor strength and thus the reliability [20], the associated increase of air gap reluctance requires the use of thicker PMs to maintain the air gap flux density so as to maintain output torque and power.

On the other hand, the poor thermal conductivity of carbon fibre sleeve will deteriorate the rotor cooling condition [21], which may cause rotor overheating and irreversible PM demagnetization at high temperatures [22]. Because of the thermal dependence of the material characteristics, the rotor stress varies with the rotor temperature [23]. Meanwhile, the temperature rise of a machine is mainly determined by the power losses and the effectiveness of the cooling system [24]. Therefore, it is obvious that the design of HSPMMs involves the multiphysics design such as electromagnetic field, rotor stress, rotor dynamics, and thermal field [25]. To get a reasonable scheme for HSPMMs under multiphysics constraints, several multidisciplinary design methods have been performed [26]-[29]. Due to the complexity of multiphysics design affected by many factors, only part of the multiphysics design process is discussed in detail in these multiphysics designs. The influence of some design parameters on multiphysics performance has not been studied in detail, including the effects of PM material, rotor diameter and PM thickness on rotor stress distribution, and the effects of impeller mass, bearing support stiffness, and rotor design parameters on rotor critical speed. At the same time, the temperature-mechanical coupling relationship is also ignored in the multiphysics designs. A complete and detailed multiphysics design process is missing in the existing multiphysics design, which would make it difficult to obtain high-reliability design solutions for designers of HSPMM, especially most designers without rich experience.

Therefore, in this paper, a detailed and complete multiphysics design process is presented for an HSPMM to obtain high-reliability design parameters. Firstly, the initial design is obtained through electromagnetic and mechanical design theory. Then, the influence of design parameters on rotor stress is analyzed in detail, including PM material, rotor temperature, sleeve thickness, PM thickness and rotor diameter. Furthermore, the rotor dynamics have also been

studied in detail, including the effects of bearing stiffness, impeller mass, rotor diameter, core length, and gyroscopic effect on critical speed. The parameters of the active part of the rotor are further limited through the analysis of rotor stress and dynamics. Based on the limitations of the parameters, the comprehensive research on the electromagnetic field and the loss characteristics are implemented to obtain a good electromagnetic performance. Afterwards, the cooling system is designed and the thermal field is also studied based on the fluid-temperature coupling model in Ansys-Cfx. Considering the interactions between mechanical and thermal characteristics, the temperature-stress coupling model is established to obtain more accurate results. Finally, one 400 kW, 10 000 rpm HSPMM is fabricated based on the above procedures, and the test results demonstrate the detailed multiphysics design process is feasible. The presented complete and detailed multiphysics design process in this paper would provide a valuable reference for designers of HSPMMs to obtain a reliable and robust design, especially most designers without rich experience.

II. Initial Design

The determination of initial design dimensions is the first step in the design. Based on a 400 kW, 10 000rpm HSPMM, the preliminary determination of key parameters is introduced in detail by considering the comprehensive performance of the HSPMM.

For the HSPMG, the rotor stress σ is limited to be less than the tensile strength of the rotor material [30]:

$$\sigma = \rho v^2 \le \frac{[\sigma]}{S} \tag{1}$$

where ρ is the density of the rotor material, v is the rotor line velocity. [σ] is the tensile strength of the rotor material, and S is the safety factor, which is usually set to 2.

The maximum rotor diameter D_{max} is obtained according to the following formula [30]:

$$D_{\max} \le \frac{2}{\omega}\sqrt{\frac{[\sigma]}{S\rho}} \tag{2}$$

For the HSPMM, stainless steel, Ti-alloy and carbon fiber are commonly used in the retaining sleeve and the material properties are shown in the Table I. 90% of the rotor weight is steel, so we take the rotor density as 7850 kg/m^3. The tensile strength of stainless steel, Ti-alloy and carbon fiber sleeve is 520 MPa, 895 MPa and 1400 Mpa, respectively.

TABLE I
Material Properties of Different Sleeves

Name	Density (kg/m^3)	Permissible stress (MPa)	Electronic conductivity (10^5 S/m)
Steel	7 850	520	12
Ti-alloy	4 400	895	6.1
Carbon Fiber	1 620	1 400	0.3

sle
from the figure that for the carbon fiber sleeve, the rotor diameter can be designed is largest, while it is the smallest for steel sleeve. Besides, based on an identical initial design scheme, using three sleeve materials of the same thickness, their rotor eddy current losses are also analysed, as shown in Fig. 2. As can be seen from the figure, for high power HSPMMs, due to the large electrical conductivities of the Ti-alloy and steel, huge rotor eddy current losses are generated, which would not only greatly reduce the efficiency of the machine, but would also bring great difficulties to the heat dissipation of the rotor. Due to the low conductivity of the carbon fiber sleeve, the rotor eddy current loss is much smaller than that for the other two sleeves. Therefore, the carbon fiber sleeve is selected in the design. The large rotor diameter can effectively reduce the rotor length and increase the rotor dynamic. However, it has been shown that the large rotor diameter would greatly increase the rotor eddy current loss and the air friction loss in [31]. Therefore, the choice of rotor diameter must consider the balance of rotor dynamics, rotor stress and rotor loss. For the designed HSPMM, the line speed of the rotor is limited to about 150 m/s considering the reliability of the rotor, so the rotor diameter is initially selected as 260 mm.

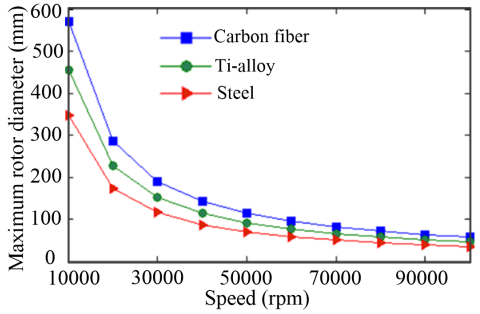

Fig. 1. Maximum rotor diameter with rotational speed at different sleeves.

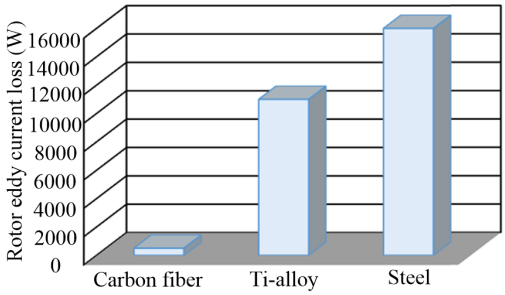

Fig. 2. Rotor eddy current loss with different sleeves.

Based on the initial rotor diameter, the core length (L_a) can be found by [31],

$$D_a^2 L_a = \frac{6.1\times10^4}{a_p k_{Nm} K_{dp} A B_\delta} \cdot \frac{p}{n_N} \tag{3}$$

where D_a is the stator inner diameter, which is only two air gaps larger than the rotor diameter. p is the power, a_p is the PM pole arc coefficient, K_{Nm} is the gap flux factor, K_{dp} is the winding factor, A is the electric load, B_δ is the air gap flux density, n_N is the rated speed.

For HSPMM, the air gap length has a great effect on the air friction loss. Air friction loss is usually calculated by the following empirical equation [16]

$$\begin{cases} p_{air} = KC_f \pi \rho \omega^3 r^4 L_a \\ C_f = \dfrac{0.0152}{R_{e\delta}} \left[1 + \left(\dfrac{32 R_{ea}}{7 R_{e\delta}} \right)^2 \right]^{0.38} \\ R_{e\delta} = \dfrac{\rho \omega r \delta}{\mu} \\ R_{ea} = \dfrac{\rho v_a 2\delta}{\mu} \end{cases} \quad (4)$$

where K is the roughness coefficient, the value is 1.0 for smooth surfaces and 2.5 for axially slotted surface, ρ is the air density, ω is the angular velocity, L_a is the core length and r is the rotor radius, C_f is the friction coefficient of air, $R_{e\delta}$ and R_{ea} are the tangential Reynolds number and the axial Reynolds number, respectively, δ is the air gap length, v_a is the average axial velocity and μ is the air dynamic viscosity. In addition, in order to maintain the same air gap flux density, a large air gap would increase the PM thickness. Fig. 3 shows the effect of air gap length on air friction loss and PM thickness. As seen, a large air gap length can effectively reduce air friction loss, while also reducing assembly difficulties. But a large air gap would increase the PM thickness. By considering air friction loss, assembly and PM thickness, the air gap length is determined to be 3 mm in the design.

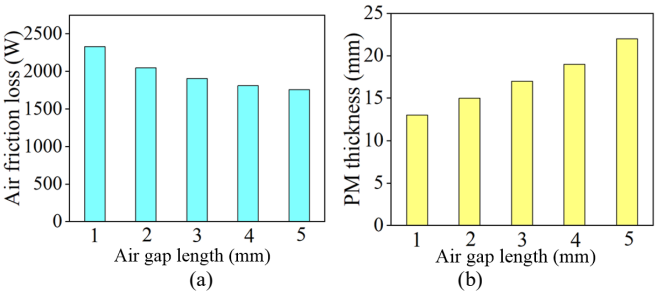

Fig. 3. Air friction loss and PM thickness with air gap length.

Based on the above analysis, the main design specifications of the HSPMM are given in Table II. A 4-pole rotor and 48-slot stator HSPMM is designed, and the surface-mounted SmCo PM is used because of its higher operating temperature and lower temperature demagnetization coefficient than NdFeB PM in this paper. Cooling paths are introduced in the stator slots and shell to improve the heat dissipation condition. The initial values of the number of conductors per slot and PM thickness can be obtained as 6 and 13 mm, respectively. At the same time, the maximum sleeve thickness is set as 7 mm to improve the heat transfer characteristics of the rotor.

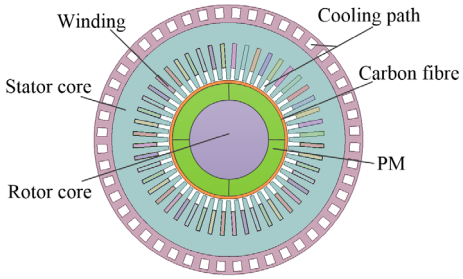

Fig. 4. Structure of HSPMM.

TABLE II
Initial sizes of the HSPMM

Name	Value
Pole number	4
Rotor diameter (mm)	260
core length (mm)	230
Stator slots	48
Air gap length (mm)	3
Pole arc coefficient	1
Retaining sleeve	Carbon fiber
Number of conductors per slot	6
PM thickness (mm)	13
Sleeve thickness (mm)	7

After the determined, th determine the to ensure the rotor safety at high speeds, the tangential stress of the sleeve and PMs should be smaller than their maximum permissible tensile strengths. For the designed HSPMM by considering any tolerance margins, the constraint condition for the rotor stress at 1.2 times the rated speed is expressed as

$$\begin{cases} \sigma_{tp} < 30 \text{ MPa} \\ \sigma_{ts} < 1000 \text{ MPa} \end{cases} \quad (5)$$

where σ_{tp} is the stress of PMs, and σ_{ts} the stress of sleeve.

In this analysis, the NdFeB and SmCo PM materials are employed and their material properties are listed in Table III. It is known that the temperature of the rotor has a great influence on the rotor stress distribution. In this design, the maximum temperature of the rotor is limited to 130 ºC in order to ensure the reliability of the rotor. Therefore, in the calculation of the rotor stress, the rotor temperature is assumed to be 130 °C and the interference between the sleeve and the PM is 0.1 mm. The rotor stress distribution under two PM materials can be obtained by 3D finite element analysis (FEA), as shown in Figs. 5-6. It can be seen that the sleeve stress under the both PMs is far lower than the maximum tensile strength of the carbon fiber. However, the stress of the two PMs exceeds the maximum tensile strength of the corresponding PM material.

TABLE III
MATERIAL PROPERTIES OF THE ROTOR

Material property	Rotor core	SmCo	NdFeB	Carbon Fiber Tangential	Ra
Density (kg/m^3)	7 850	7400	7 400	1 620	
Elastic modulus (GPa)	206	160	160	182	8.
Poisson's ratio	0.31	0.24	0.24	0.28	0.
Temperature expansion coefficient (μm/m/ºC)	11	11	5	-0.2	35

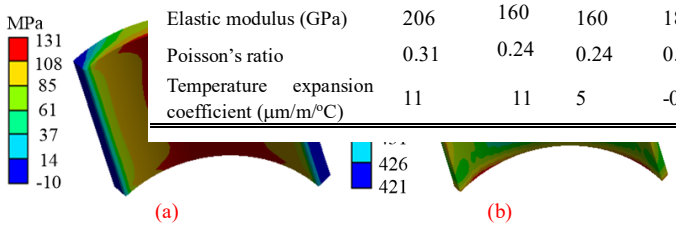

Fig. 5. Rotor stress with NdFeB PM. (a) PM stress. (b) Sleeve stress.

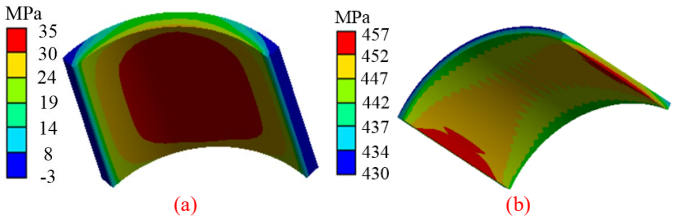

Fig. 6. Rotor stress with SmCo PM. (a) PM stress. (b) Sleeve stress.

It is clear that the operating temperature has a great effect

on the rotor stress. Under two PM materials, the change in rotor stress with operating temperature is also shown in Fig. 7. It is seen, as the operating temperature increases, the sleeve and PM stress would increase sharply.When the temperature reaches about 80 ºC, the PM stress can no longer meet the requirements of the rotor strength. It is seen, the effect of rotor temperature on the SmCo PM stress is much smaller than that on the NdFeB PM stress due to the large temperature expansion coefficient of SmCo PM. Therefore, in this design, in order to improve the rotor stress at the high temperature, SmCo PM is used.

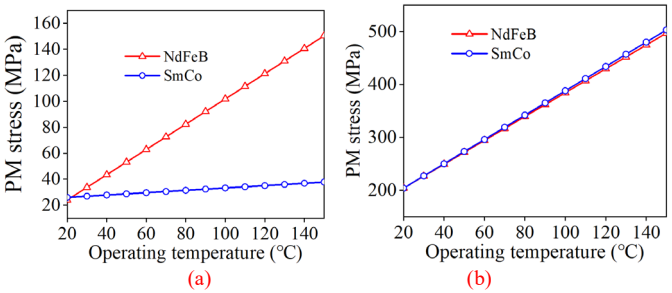

Fig. 6. Rotor stress with operating temperature under both PMs. (a) PM stress. (b) Sleeve stress.

The rotor stress with sleeve thickness and PM thickness at same rotor diameter are also analysed by 3D finite element analysis, as shown in Fig. 7. It is indicated that the sleeve thickness has a great effect on the rotor stress, while the PM thickness has a small effect on the rotor stress. In the rotor stress analysis, the effect of the PM thickness on the rotor stress can be ignored. Moreover, while the corresponding requirements for the sleeve stress can be readily met, it is difficult to meet the requirement for the PM stress. In order to meet the rotor stress, the variation of rotor stress with rotor diameter and sleeve thickness is also carefully investigated, as shown in Fig. 8. For sleeve stress, the effect of the rotor diameter is much greater than the sleeve thickness. However, for PM stress, both the sleeve thickness and the rotor diameter have a large effect.

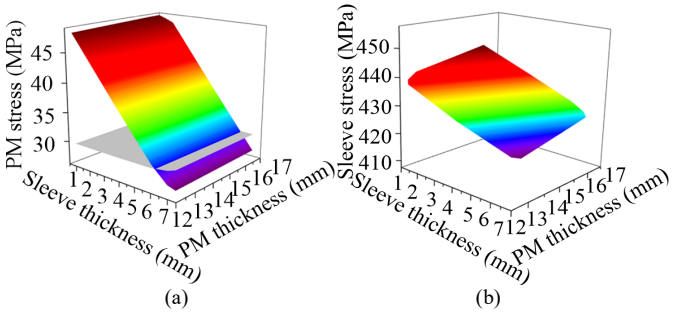

Fig. 7. Rotor stress with sleeve thickness and PM thickness. (a) Tangential stress of PMs. (b) Tangential stress of sleeve.

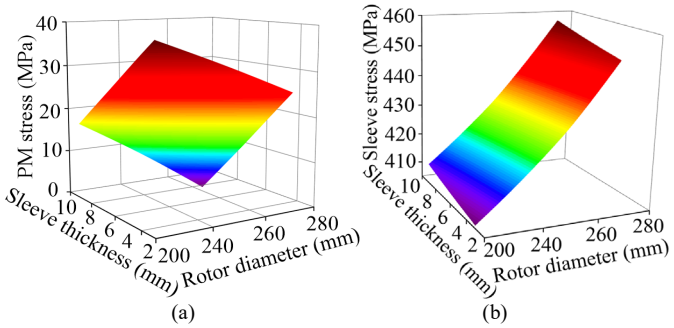

Fig. 8. Rotor stress with sleeve thickness and rotor diameter. (a) Tangential stress of PM. (b) Tangential stress of sleeve.

The combination of the rotor diameter and the sleeve thickness to meet the rotor stress requirements is also shown in Fig. 9. As shown, when the maximum sleeve thickness is maintained at 7 mm, to meet the requirements of the rotor stress, the rotor diameter should be less than 240 mm.

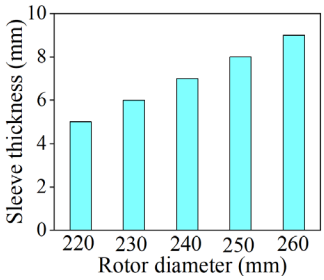

Fig. 9. The combination of the rotor diameter and the sleeve thickness to meet the rotor stress requirements.

IV. Rotor Dynamic Analysis

While the rotor diameter is limited by the stress at the maximum speed, the core length can be further limited by the critical speed. When the rotor speed is close to its critical speed, the rotor would resonate and suffer serious damage. To avoid this, the maximum speed, n_s, should be limited by [32]

$$n_s < 0.75 n_{cr1} \tag{6}$$

where n_{cr1} is the first critical speed.

For the HSPMM, the maximum speed is 11 000 rpm and the rotor should be designed with the required first critical speed higher than 14 667 rpm according to (6). A 3D FEA model with impeller is established in Ansys-Modal in this paper, as shown in Fig. 10. In the 3D FEA, the bearings are modelled as springs and the rated speed is set to consider the gyroscopic effect produced by the rotation of the rotor.

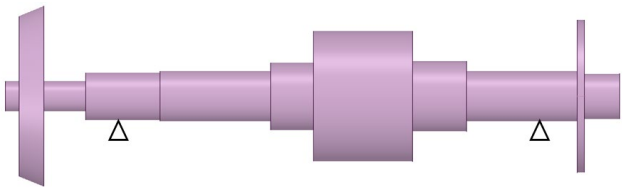

Fig. 10. The 3D FEA model for critical speed.

A magnetic bearing is employed in the HSPMM. The effect of bearing support stiffness on critical speed is analyzed in the range 10^5 to 10^9 N/m, as show in Fig.11. It is obvious that the critical speed of the first-order mode and the second-order mode increases sharply with the increase of bearing stiffness.

When the support stiffness is greater than 10^8 N/m, the first-order and second-order modes tend to stabilize. But at this time, the critical speed of higher order would increase sharply. Therefore, it is clear that the bearing support stiffness has a great influence on the critical speed, and the appropriate bearing support stiffness should be designed to avoid rotor resonance. In addition, the influence of the impeller mass on the bending critical speed of the rotor is also analyzed, as shown in Fig. 12. It can be seen from the figure, as the impeller mass increases, the bending critical speed gradually decreases, and then stabilizes. Therefore, proper impeller quality is also critical for the design of rotor dynamics.

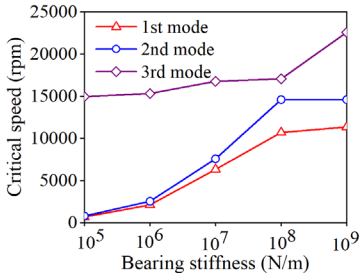

Fig. 11. Critical speed with bearing stiffness.

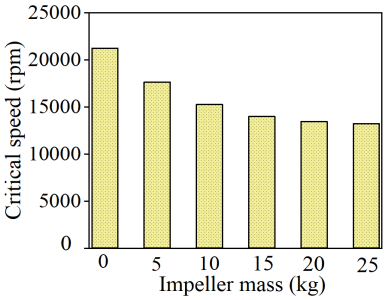

Fig. 12. Critical speed with impeller mass.

Fig. 13 shows the bending critical speed versus rotor diameter and core length. It is obvious, the influence of the core length on the critical speed is far greater than the influence of the rotor diameter on it. Fig.14 shows the relationship between the core length and rotor diameter under the bending critical speed meeting the critical speed constraint. It is seen that the larger the rotor diameter, the smaller the core length that meets the critical speed requirements. According to the previous analysis of rotor stress, the maximum rotor diameter is limited to 240 mm. Therefore, at the limit of the maximum rotor diameter, the required core length is 270 mm. Therefore, in order to improve the rotor dynamic characteristics, the core length should be limited to less than 270 mm to meet the requirement of critical speed.

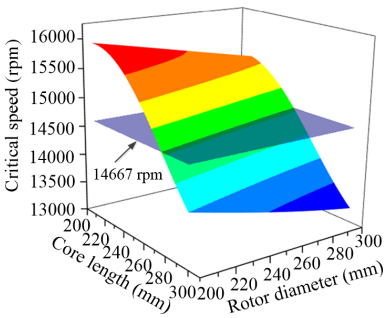

Fig. 13. First critical speed at different rotor diameters and core lengths.

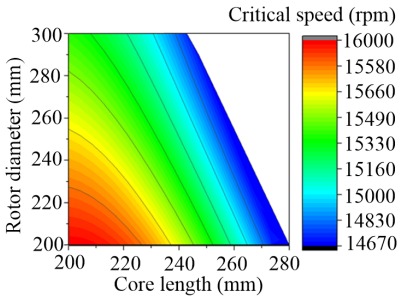

Fig. 14. Relationship between the core length and rotor diameter meeting the critical speed constraint.

V. Determination of the Main Parameters by Electromagnetic Analysis

Based on the above analysis, the design ranges of the rotor diameter and core length are refined. More specific design solutions of the HSPMM should be further determined based on electromagnetic characteristics analysis.

A. Rotor Diameter and Core Length

For the given PM thickness of 13 mm and 6 conductors per slot, the electromagnetic characteristics of the HSPMM versus the rotor diameter and core length are calculated by using Ansys-Maxwell, as shown in Table IV.

In the process, the iron loss and rotor eddy current loss are obtained by using the 2D FEM. The stator core is laminated using 0.35 mm steel sheets and the conductivities of carbon fiber, PM, and rotor core are 2×10^4 S/m, 1.1×10^6 S/m, and 2×10^6 S/m, respectively. At the same time, the air friction loss can be obtained by the empirical formula provided in [16]. The AC copper loss at high frequency is obtained by using eddy current field [12]. It is seen, as the increase of the rotor diameter, the friction loss and eddy current loss increase gradually, and the efficiency decreases gradually. Therefore, small rotor diameter can reduce rotor loss and improve machine efficiency.

TABLE IV
ELECTROMAGNETIC PERFORMANCE WITH ROTOR DIAMETER

Rotor diameter (mm)	200	220	240
Core length (mm)	266	246	232
Output power (kW)	400	400	400
Line voltage (V)	422	421	423
Rotor eddy current loss (W)	521	665	806
Air friction loss (W)	3 854	4 462	4 822
Iron loss (W)	5 781	7 638	8 752
Copper loss (W)	1 642	1 579	1 416
Efficiency (%)	97.1	96.6	96.3

mm. As shown, a large PM thickness reduces the rotor core length, thereby improving rotor dynamics. A large core long is required to obtain the required output power when a thin PM is used. If the PMs are too thin, the required core length would be larger than the limited value, which would result in faulty rotor dynamics. Therefore, a suitable PM thickness should be selected by balancing electromagnetic characteristics and rotor dynamics.

TABLE V
ELECTROMAGNETIC PERFORMANCE WITH THE PM THICKNESS

PM thickness (mm)	12	13	14	15	16	17
Core length (mm)	260	252	247	242	238	234
Air gap flux (T)	0.45	0.47	0.48	0.49	0.50	0.51
Output power (kW)	400	400	400	400	400	400
Back EMF (V)	536	525	513	504	499	491
Line voltage (V)	420	421	421	420	421	420
Rotor eddy current loss (W)	512	526	532	536	542	545
Iron loss (W)	5 488	5 514	5 531	5 546	5 559	5 573
Efficiency (%)	96.78	96.77	96.76	96.75	96.74	96.73

C. Number

Since the d
HSPMM, the
4, 6, or 8. Ta
versus the number of conductors per slot. In this study, the rotor diameter is set to 220 mm and the PM thickness 15 mm. It is seen, the required core length is up to 330 mm when the number of conductors per slot is 4, which would lead to rotor resonance. Although choosing a large number of conductors per slot, say 8, can reduce the core length, this may cause a large thermal load and a high temperature rise. At the same time, the higher voltage regulation rate would be generated with the number of conductor per slot 8.

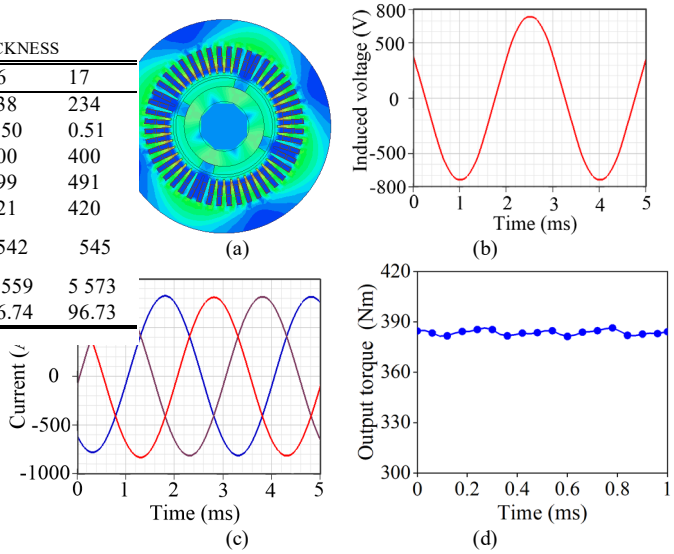

Fig. 15. Electromagnetic performance. (a) The flux density distribution. (b) Induced EMF at no load. (c) Phase current at full load. (d) Output touqre.

TABLE VI
ELECTROMAGNETIC PERFORMANCE WITH THE NUMBER OF CONDUCTOR PER SLOT

The number of conductor per slot	4	6	8
Core length (mm)	330	240	200
Output power (kW)	407	405	403
Back EMF (V)	472	518	580
Line voltage (V)	428	425	421
Current density (A/mm^2)	1.9	2.8	3.8
Rotor eddy current loss (W)	773	562	467
Iron loss (W)	8 817	6 545	5 720
Copper loss (W)	890	1 598	2 727
Efficiency (%)	96.5	96.8	96.8

D. Electrom

Based on
electromagneti
dynamics, an
the HSPMM,
simulation in the 2D FEA of Ansys-Maxwell, the electromagnetic performance of the HSPMM is analyzed, as shown in Fig. 15. Fig. 15 (a) shows the flux density distribution over the machine cross section. The root mean square (RMS) of induced EMF is 520 V at no load as shown in Fig. 15 (b). Fig. 15 (c) shows the phase current waveform at full load with the RMS value of 563 A. The output torque is 385 Nm as shown in Fig.15 (d).

The iron loss can be obtained by the classic Bertotti loss separation model by

$$P_{Fe} = P_h + P_c + P_e = K_h f B_m^{\alpha} + K_c f^2 B_m^2 + K_e f^{1.5} B_m^{1.5} \quad (7)$$

where P_h, P_c, and P_e denote the hysteresis loss, eddy current loss, and excessive loss, respectively, K_h, K_c, and K_e the corresponding coefficients, f the fundamental frequency of the magnetic field, and B_m the flux density amplitude.

TABLE VII
KEY PARAMETERS OF THE HSPMM

Name	Value
Rotor diameter (mm)	215
Stator diameter (mm)	393
Core length (mm)	242
Conductors per slot	6
Sleeve thickness (mm)	7
PM thickness (mm)	15
Stator slot number	48

s coefficients can be obtained by the core loss per
f core mass at different frequencies provided by the
rer, where $k_h = 0.019$, $\alpha = 1.83$, $k_c = 4.5 \times 10^{-5}$ and
10^{-6}. Based on the above analysis, the iron loss at
peed can be obtained as 6 707 W.

m-wound windings, the skin and proximity effects
equency greatly increase the winding loss. To
such effects, the model of each conductor is
l by eddy current field simulation in Ansys Maxwell.
gn, 48 wires of width 5 mm and thickness 1.2 mm
er slot. The AC winding loss at the rated frequency can be obtained by eddy current field simulation as 1 782 W.

The rotor eddy current loss can be obtained based on Ansys Maxwell transient FEM. The rotor eddy current loss under rated operation can be obtained as 542 W. At the same time, the air friction loss can be also obtained as 4 280 W by the empirical formula [16]. Therefore, the efficiency of the HSPMM can be obtained as 96.7%.

VI. THERMAL ANALYSIS AND COUPLED TEMPERATURE-STRESS ANALYSIS

A. Thermal Analysis

The thermal analysis is a very important part in the design procedure of HSPMMs. To guarantee a safe operation of the HSPMM, the maximum working temperatures of the winding and rotor are both set as 130 °C. The cooling path is set in the stator slot and shell to improve the thermal transfer of HSPMM, which has been shown in Fig. 4. According to the symmetry, a 1/4 cross sectional model of the HSPMM is taken as the solution domain in the Ansys-Cfx. The turbulence model is employed in this study with the inlet velocity set as 2.5 m/s and the inlet temperature as 30 °C. The rotor and shaft are set to rotate at the rated speed since the rotor rotating speed influence the fluid flow, as shown in Fig.16 (a). Fig. 16 (b) shows the calculated temperature distribution of HSPMM with the maximum stator temperature of 123 °C occurring in the middle of the stator winding, and the

maximum rotor temperature of 108 ºC occurring in the middle of the rotor. The operating temperatures in all parts are below the limit.

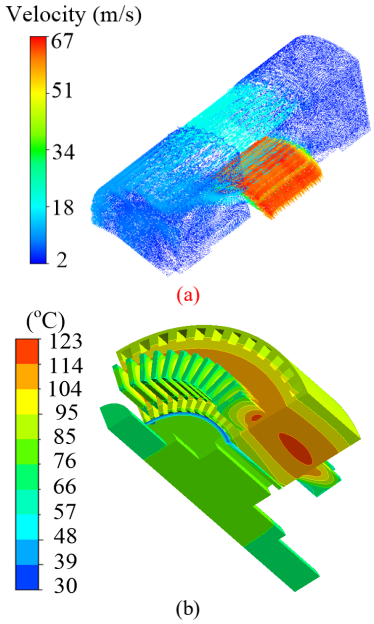

Fig. 16. Fluid velocity distribution and temperature distribution of the whole machine. (a) Fluid velocity distribution. (b) Temperature distribution.

B. *Coupled Temperature-Stress Analysis*

In the previous rotor stress analysis, since a constant rotor temperature is assumed, some error has been produced in comparison to using the actual value. Therefore, the rotor stress should be calculated once again at 1.2 times rated speed by the coupled temperature-stress model so as to obtain more accurate results. In this analysis, the rotor temperature distribution is obtained through the previous thermal analysis, which can be coupled through temperature-stress coupling analysis in Ansys-Workbench. Fig. 17 shows the rotor stress distribution obtained by the coupling analysis. It can be seen that the maximum PM stress is 28 MPa and the maximum sleeve stress is 461 MPa. They all meet the tensile strength of the corresponding material and reserve a certain safety margin.

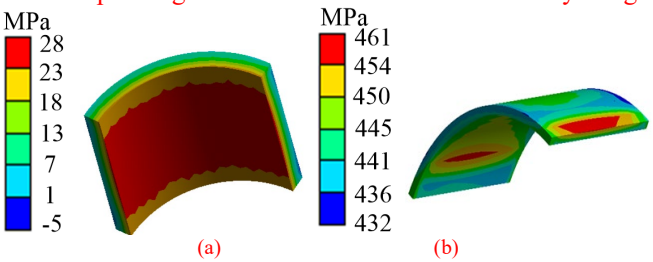

Fig. 17. Rotor stress by coupled temperature-stress model. (a) PM stress. (b) Sleeve stress.

C. *Rotor Dynamic Analysis*

For the final designed HSPMM, the mode of oscillation and critical speed with impeller must be checked through 3D FEA. In the final design, the impeller mass is 15 kg and the bearing stiffness of magnetic bearing is 5×10^6 N/m. Fig. 18 shows the first bending mode and second bending mode. Considering the influence of the gyroscopic effect brought by the rotor rotation on the critical speed, the natural frequency of the rotor with the operating speed is also obtained, as shown in Fig.19. In the figure, the first one is cylindrical mode, the second one is conical mode, and the third one is bending mode. The bending mode is generally considered to be the critical speed. It is seen, the natural frequency of bending mode considering the gyroscopic effect is 249 Hz, and the corresponding critical speed is 14 924 rpm. The value of 0.75 n_{cr1} is 11 193 rpm and it is larger than the rated speed 10 000 rpm, which proves that the rotor would not resonate in the entire speed operating range.

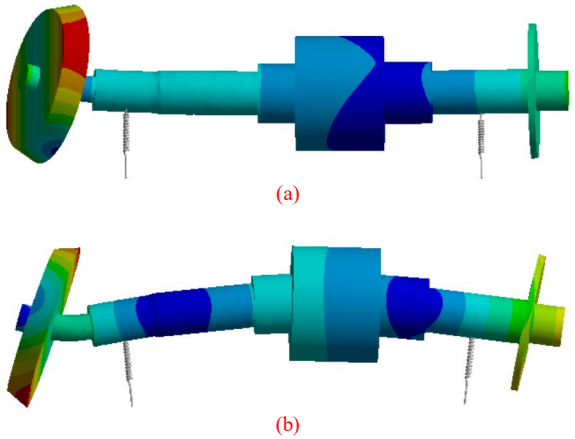

Fig. 18. Modes of oscillation. (a) First bending mode. (b) Second bending mode.

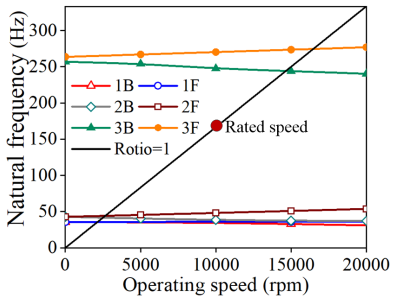

Fig. 19. Natural frequency of the rotor with rotor operating speed.

VII. Experimental Tests

According to the above design, a 400 kW 10 000 rpm HSPMM prototype has been manufactured. Fig. 20 shows two photos of the prototype. Fig. 21 shows a photo of the testbed.

Fig. 20. The prototype. (a) Rotor. (b) Stator.

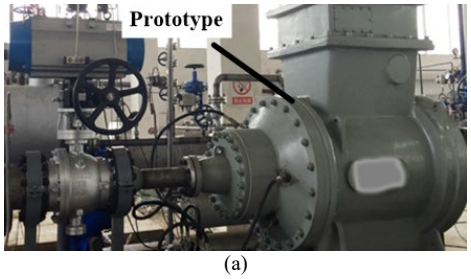

(b) (c)

Fig. 21. The test facilities. (a) Experimental platform. (b) Voltage sensor. (c) Current sensor.

To evaluate the performance, the prototype is firstly driven as a motor by a power electronic converter. Fig.22 (a) illustrates the measured no-load line voltage waveform at 10 000 rpm, and Fig.22 (b) the no load line voltage at different speeds. As shown, the measured no load voltage per phase at the rated speed is 528 V, and the relationship between voltage and speed is linear with a slope of about 0.05 V/rpm.

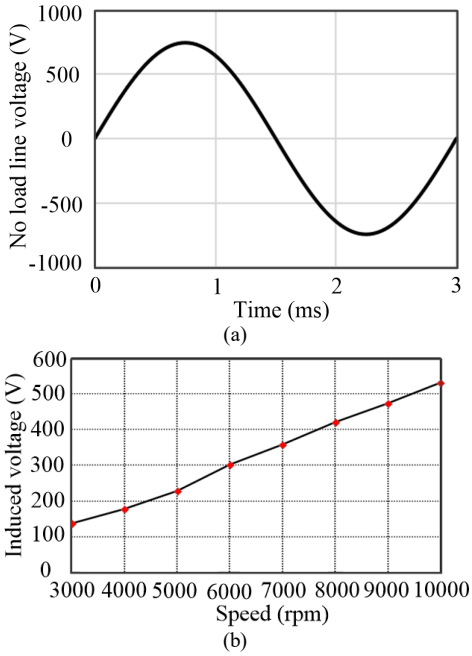

Fig. 22. Experimental results at no load. (a) Phase voltage waveform at 10 000 rpm no load. (b) No-load line voltage versus speed.

In the full load test, the generating power is sent to the power grid through the converter. The measured voltage and current at full load operation are shown in Fig.23. The RMS values of full load voltage and current measured by high-frequency sensors are 423 V and 574 A, respectively, which are in good agreement with the simulation results by the 2D FEA model. The outpower power of the HSPMM can be got by the power analyser. The measured efficiency is 96.3%, showing the excellent electromagnetic design of HSPMM. The temperature distribution on the stator is also measured. Specifically, the stator temperature is measured by Pt100 resistance temperature detector installed in the winding. The stable stator temperature measured by full load test after 100 minutes is 118 °C, which is very close to the calculated result. Key experimental parameters in comparison to simulations from multiphysics analysis have been summarized in Table VIII. As can be seen from Table VIII, the experimental results agree well with the theoretical analysis.

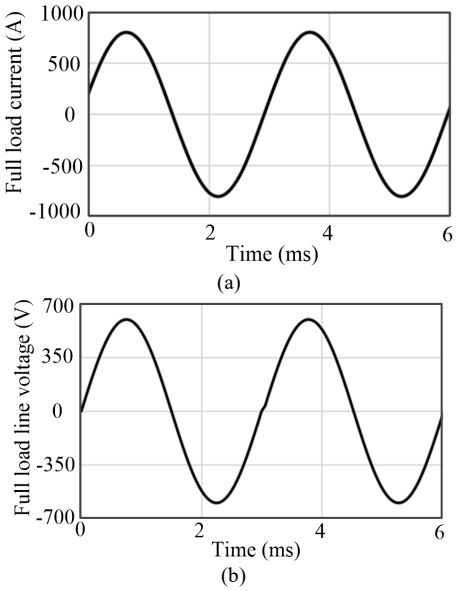

Fig. 23. Measured (a) current and (b) voltage waveform at full load operation.

TABLE VIII
EXPERIMENTAL AND CALCULATED RESULTS

Name	Measurement	Calculation
Efficiency (%)	96.3	96.7
No oad line voltage (V)	528	521
Full oad phase current (A)	572	563
Winding temperature (°C)	118	123

completed, including the initial scheme, rotor stress, rotor dynamics, loss and electromagnetic characteristics, temperature characteristics, and temperature-stress coupling models. The comprehensive numerical simulation and experimental test results of the full-size prototype agreed well with each other, confirming the effectiveness of the design process for HSPMMs. Some key points are summarized as follows.

1) Ti-alloy and steel sleeves are not suitable for high power HSPMMs due to huge rotor eddy current loss. Small mechanical air gap length would cause huge air friction loss.

2) The effect of rotor temperature on the SmCo PM stress is much smaller than that on the NdFeB PM stress due to the large temperature expansion coefficient of SmCo PM. The effect of the PM thickness on the rotor stress is very small. A large rotor diameter would result in a large sleeve thickness.

3) The influence of the core length on the critical speed is much greater than the influence of the rotor diameter on it. The bearing support stiffness has a great influence on the critical speed, and the appropriate bearing support stiffness should be designed to avoid rotor resonance. As the impeller mass increases, the bending critical speed gradually decreases, and then stabilizes.

4) A large rotor diameter would cause large rotor loss and reduce machine efficiency. A large number of conductors per slot can greatly reduce the core length, while it would greatly increase the thermal load of the HSPMM. Also, increasing the PM thickness can also effectively reduce the core length.

5) The temperature-stress coupling model was established to obtain accurate rotor stress distribution by considering the interactions between mechanical and thermal characteristics.

REFERENCES

[1] D. Gerada, A. Mebarki, N. L. Brown, C. Gerada, A. Cavagnino, A. Boglietti, "High-speed electrical machines: technologies, trends, and developments," *IEEE Trans. Ind. Electron.*, vol. 61, no. 6, pp. 2946-2959, Jun. 2014.

[2] A. Borisavljevic, H. Polinder, J.Abraham Ferreira, "On the speed limits of permanent-magnet machines," *IEEE Trans. Ind. Electron.*, vol. 57, no. 1, pp. 220-227, Jan. 2010.

[3] N. Bianchi, S. Bolognani, and F. Luise, "Potentials and limits of high-speed PM motors," *IEEE Trans. Ind. Appl.*, vol. 40, no. 6, pp. 1570-1578, Nov./Dec. 2004.

[4] A. Boglietti, A. Cavagnino, A. Tenconi, et al, "Key design aspects of electrical machines for high-speed spindle applications," *36th Annual Conference of the IEEE Industrial Electronics Society*, pp. 1735-1740, 2010.

[5] J. F. Gieras and J. Saari, "Performance calculation for a high-speed solid-rotor induction motor," *IEEE Trans. Ind. Electron.*, vol. 59, no. 6, pp. 2689-2700, Jun 2012.

[6] N. Uzhegov, A. Smirnov, C. H. Park, J.H. Ahn, J. Heikkinen, J. Pyrhonen, "Design aspects of high-speed electrical machines with active magnetic bearings for compressor applications," *IEEE Trans. Ind. Electron.*, vol. 64, no. 11, pp. 8427-8436, Nov. 2017.

[7] G. H. Du, N. Huang, "Friction loss and thermal analysis of a high-speed permanent magnet machine for waste heat power generation application," *IEEE Access*, vol. 7, pp. 131710–131718, Sep. 2019.

[8] N. Uzhegov, J. Barta, J. Kurfürst, C. Ondrusek, J. Pyrhönen, "Comparison of high-speed electrical motors for a turbo circulator application," *IEEE Trans. Ind. Appl.*, vol. 53, No. 5, pp.4308-4317, Sep. 2017.

[9] Z. Kolondzovski, A. Arkkio, J. Larjola, P. Sallinen, "Power limits of high-speed permanent-magnet electrical machines for compressor applications," *IEEE Trans. Energy Conversion*, vol. 26, no. 1, pp. 73-82, Mar. 2011.

[10] A. Tenconi, S. Vaschetto, A. Vigliani, "Electrical machines for high-speed applications: design considerations and tradeoffs," *IEEE Trans. Ind. Electron.*, vol. 61, no. 6, pp. 3022-3029, Jun. 2014.

[11] F. G. Zhang, G. H. Du, T. Y. Wang, G. W. Liu, W. P. Cao, "Rotor retaining sleeve design for a 1.12-MW high-speed PM machine," *IEEE Trans. Ind. Appl.*, vol. 51, no. 5, pp. 3675-3685, Sept./ Oct. 2015.

[12] G. H. Du, W. Xu, J. G. Zhu, N. Huang. "Power loss and thermal analysis for high power high speed permanent magnet machines," *IEEE Trans. Ind. Electron.*, vol. 67, no. 4, pp. 2722-2733, Apr. 2020.

[13] O. Aglen, A. Andersson, "Thermal analysis of a high-speed generator," *38th IAS Annual Meeting: Crossroads to Innovation,* Oct.12-16, pp. 547-554, 2003.

[14] D. A. Gonzalez, D. M. Saban, "Study of the copper losses in a high-speed permanent-magnet machine with form-wound windings," *IEEE Trans. Ind. Electron.*, vol. 61, no. 6, pp. 3038-3045, Jun. 2014.

[15] M. Nakano, H. Kometani, and M. Kawamura, "A study on eddy-current losses in rotors of surface permanent-magnet synchronous machines," *IEEE Trans. Ind. Appl.*, Vol. 42, No. 2, pp. 429-435, Mar./Apr. 2006.

[16] Z. Y. Huang, J. C. Fang, X. Q. Liu, B. C. Han "Loss calculation and thermal analysis of rotors supported by active magnetic bearings for high-speed permanent-magnet electrical machines," *IEEE Trans. Ind. Electron.*, vol. 63, no. 4, pp. 2027-2035, Apr. 2016.

[17] A. Binder, T. Schneider and M. Klohr, "Fixation of buried and surface-mounted magnets in high-speed permanent-magnet synchronous machines," *IEEE Trans. Ind. Appl.*, Vol. 42, No. 4, pp. 1031-1037, July/Aug. 2006.

[18] W. L. Li, H. B. Qiu, X. C. Zhang, J. C. Cao, S.N. Zhang, R. Yi, "Influence of rotor-sleeve electromagnetic characteristics on high-speed permanent-magnet generator," *IEEE Trans. Ind. Electron.*, vol. 61, no. 6, pp. 3030-3037, Jun. 2014.

[19] Y. Zhang, S. McLoone, W. P. Cao, F. Qiu, C. Gerada, "Power Loss and Thermal Analysis of a MW High Speed Permanent Magnet Synchronous Machine," *IEEE Trans. Energy Conversion*, vol. 32, no. 4, pp. 1468-1478, May. 2017.

[20] D. K. Hong, B. C. Woo, D. H. Koo, "Rotordynamics of 120000 r/min 15 kW ultra high speed motor," *IEEE Trans. on Magnetic*, vol. 60, no. 2, pp. 2831-2834, Feb. 2009.

[21] H. B. Qiu, R. Yi, W. L. Li, N. Jin, "Influence of rectifiers on high-speed permanent magnet generator electromagnetic and temperature fields in distributed power generation systems," *IEEE Trans. Energy Conversion*, Vol. 30, Issue: 2, pp. 655-662, Jun. 2015.

[22] G. H. Du, W. Xu, J. Zhu, N. Huang, "Rotor stress analysis for high speed permanent magnet machines considering assembly gap and temperature gradient," *IEEE Trans. Energy Conversion*, Early Access, Sep. 2019.

[23] W. L. Li, X. C. Zhang, S. Cheng, J. Cao, "Thermal optimization for a HSPMG used for distributed generation systems," *IEEE Trans. Ind. Electron.*, vol. 60, no. 2, pp. 474-482, Feb. 2013.

[24] Y. Wang, J. H. Feng, S. Y. Guo, Y. F. Li, Z. C. Chen, Y. Wang, and Z. Q. Zhu, "Investigation of optimal split ratio for high-speed permanent magnet brushless machines," *IEEE Trans. Magn.*, vol. 54, no. 11, Art. no. 8105605. Nov. 2018.

[25] H. Hao, "Multi-fields analyse of high speed permanent magnet brushless motors and sensorless control strategy," Ph.D. dissertation, Zhejiang University, Hangzhou, China, 2013.

[26] Z. Y. Huang, J. C. Fang, "Multiphysics design and optimization of high-speed permanent-magnet electrical machines for air blower applications," *IEEE Trans. Ind. Electron.*, vol. 63, no. 5, pp. 2766-2774, May. 2016.

[27] N. Uzhegov, E. Kurvinen, J. Nerg, J. Pyrh¨onen, J. T. Sopanen, S. Shirinskii, "Multidisciplinary design process of a 6-slot 2-pole high-speed permanent-magnet synchronous machine," *IEEE Trans. Ind.Electron.*, vol. 63, no. 2, pp. 784-795, Feb. 2016.

[28] W. Zhao, X. Wang, C. Gerada, H. Zhang, C. Liu and Y. Wang, "Multi-physics and multi-objective optimization of a high speed pmsm for high performance applications," *IEEE Trans. on Magnetic,*, vol. 54, no. 11, pp. 1-5, Nov. 2018.

[29] F. R. Ismagilov, N. Uzhegov, V. E. Vavilov, V. I. Bekuzin, V. A. Ayguzina, "Multidisciplinary design of ultra-high-speed electrical machines", *IEEE Trans. Energy Conversion*, vol. 33, no. 3, pp. 1203-1212, Sep. 2018.

[30] F. G. Zhang, G. H. Du, T. Y. Wang, F.X. Wang, W. P. Cao, J. L. Kirtley, "Electromagnetic design and loss calculations of a 1.12-MW high-speed permanent-magnet motor for compressor applications," *IEEE Trans. Energy Conversion*, vol. 31, no. 1, pp. 132-140, Mar. 2016.

[31] X. H. Wang. Permanent Magnet Machines. Beijing, China: China Electric Power Publishing, 2011.

[32] J. F. Gieras, "Design of permanent magnet brushless motors for high speed applications," *17th International Conference on Electrical Machines and Systems (ICEMS)*, 2014.